molecules

MDPI

Article

MOF-Derived ZrO_2-Supported Bimetallic Pd–Ni Catalyst for Selective Hydrogenation of 1,3-Butadiene

Ying Liu, Lili Liu *, Leyuan Wang, Miaoliang Zang, Lei Li and Yunkai Zhang

School of Chemistry & Chemical Engineering and Environmental Engineering, Weifang University, Weifang 261061, China; liuying@wfu.edu.cn (Y.L.); 15264543037@163.com (L.W.); 13356710254@163.com (M.Z.); 15863610289@163.com (L.L.); 17753624747@163.com (Y.Z.)

* Correspondence: liulili122@126.com

Abstract: A series of MOF-derived ZrO_2-supported Pd-Ni bimetallic catalysts (PdNi/UiO-67-CTAB(n)-A500) were prepared by co-impregnation and pyrolysis at 500 °C under air atmosphere using UiO-67-CTAB(n) (CTAB: cetyltrimethylammonium bromide; n: the concentration of CTAB; n = 0, 3, 8, 13, 18) as a sacrificial template. The catalytic activity of PdNi/UiO-66-CTAB(n)-A500 in 1,3-butadiene hydrogenation was found to be dependent on the crystal morphology of the UiO-67 template. The highest activity was observed over the PdNi/UiO-67-CTAB(3)-A500 catalyst which was synthesized using UiO-67-CTAB(3) with uniform octahedral morphology as the template for the 1,3-butadiene selective hydrogenation. The 1,3-butadiene conversion and total butene selectivity were 98.4% and 44.8% at 40 °C within 1 h for the PdNi/UiO-67-CTAB(3)-A500 catalyst, respectively. The catalyst of PdNi/UiO-67-CTAB(3)-A500 can be regenerated in flowing N_2 at 200 °C. Carbon deposited on the surface of the catalyst was the main reason for its deactivation. This work is valuable for the high-efficiency bimetallic catalyst's development on the selective hydrogenation of 1,3-butadiene.

Keywords: MOF-derived; ZrO_2; bimetallic catalysts; Pd–Ni catalysts; hydrogenation of 1,3-butadiene

Citation: Liu, Y.; Liu, L.; Wang, L.; Zang, M.; Li, L.; Zhang, Y. MOF-Derived ZrO_2-Supported Bimetallic Pd–Ni Catalyst for Selective Hydrogenation of 1,3-Butadiene. *Molecules* **2024**, *29*, 2217. https://doi.org/10.3390/molecules29102217

Academic Editor: Isidro M. Pastor

Received: 19 March 2024
Revised: 1 May 2024
Accepted: 7 May 2024
Published: 9 May 2024

1. Introduction

C_4 olefin is an important raw material for the synthesis of polymers [1,2]. However, the C_4 olefin stream from petroleum cracking contains a trace amount of 1,3-butadiene, which can severely reduce the quality of polymers and easily poison the catalysts for polymerization [2–4]. The selective hydrogenation of 1,3-butadiene is an important industrial process to remove 1,3-butadiene from petroleum cracking [5–7]. Currently, Pd catalysts are mostly used as heterogeneous catalysts for 1,3-butadiene selective hydrogenation due to their high hydrogenation activity [8–11]. However, the scarcity and high price of Pd greatly limits its application [12]. Moreover, Pd catalysts generally have low selectivity to total butenes (1-butene, trans-2-butene, and cis-2-butene) at high 1,3-butadiene conversion due to their high hydrogen activation [6,13]. To decrease the cost of the Pd catalyst and gain the high selectivity of butenes, alloying Pd with a second metal (such as Ni, Cu, Co, etc.) and selecting suitable supports to form bimetallic supported catalysts have received considerable attention [2,4,14–17]. The addition of the second metal in bimetallic Pd-based catalysts can change the surface structure and electronic properties of Pd catalysts, decrease the adsorption capacity of butenes, and improve the selectivity to total butenes [18,19]. Bimetallic Pd-Ni [13,20,21], Pd-Cu [2], Pd-Cr [22], Pd-Au [23], and Pd-Ag [24] catalysts have been shown to have superior butene selectivity over monometallic Pd catalysts. Huang et al. [13] synthesized the Ni_1-Pd_1/ZnO catalyst by the bioreduction route using Cinnamomum Camphora leaf extract. They found that the butene selectivity (90.0%) of the bimetallic Ni_1-Pd_1/ZnO catalyst was better than that of the monometallic Pd/ZnO catalyst (46.9%) [13]. Yang et al. [2] also reported that the γ-Al_2O_3-supported Pd–Cu bimetallic catalyst displayed higher butene selectivity as compared with the monometallic Pd catalyst at the same 1,3-butadiene conversion. Huang et al. [24] reported that the Pd-Ag/ES

(ES = eggshell) catalyst displayed high butene selectivity (95.8%) at high 1,3-butadiene conversion (95%) at 45 °C. The bimetallic catalyst Au(2)Pd(1)/MIL-101(Cr) (95.7%) displayed a higher selectivity of total butenes than that of Pd/MIL-101(Cr) (35.0%) when the 1,3-butadiene conversion was about 100% [23].

In recent years, metal–organic frameworks (MOFs) have emerged as a class of promising precursors or sacrificial templates for synthesizing various porous metal oxides or carbon with complex compositions and a unique structure via pyrolysis owing to abundant intrinsic molecular metal sites, an ordered pore structure, high porosity, and an adjustable pore size [25–30]. The composition and structure of MOF derivatives can be easily realized by adjusting the precursors or sacrificial templates of MOFs, modifying the pyrolysis temperature, and changing the pyrolysis atmosphere (inert or air atmosphere) [26,29,31,32]. Moreover, the ordered pore structure of MOFs can envelop other metal salts or organic species which could further modify MOF derivatives [26,33]. Recently, MOF derivatives have been widely used in heterogeneous catalysis, especially those using MOF derivatives as a support for metal nanoparticles [34–38]. Zeng et al. [34] synthesized the hierarchical mesoporous CuO@NiO (M-CuO@NiO) catalyst using MOFs as the precursor. The M-CuO@NiO catalyst displayed excellent catalytic activity and selectivity for the deoxygenation of fatty acids [34]. The conversion of stearic acid and the selectivity of C_8-C_{18} alkanes reached 99.9% and 94.4%, respectively, which were comparable to the Pt/C catalyst [34]. Lei et al. [39] successfully synthesized M-$Co_1Y_1O_x$ (Y = Cu, Mn, Fe, and Ni) catalysts using Y-doped ZSA-1 as a precursor via pyrolysis at 350 °C. The dopants displayed a great effect on the catalytic performance for toluene catalytic destruction on Co_3O_4 derived from Co-MOF [39]. They found that M-$Co_1Cu_1O_x$ showed the most prominent activity with $T_{90\%}$ reduced 31 °C (compared to M-Co_3O_4) due to improved physical properties [39]. They also reported that Co-Mn metal oxides synthesized through the pyrolysis of Mn-doped ZSA-1 presented excellent catalytic performance for toluene catalytic oxidation [40]. Wang et al. [41] prepared the nitrogen-doped carbon material (NC-E) from ZIF-8 using a novel and simple method assisted by eutectic salts. They also prepared carbon materials NC-T from ZIF-8 using traditional calcination [41]. The NC-E-supported Pt-Sn catalyst exhibited improved electrochemical activity and stability for the ethanol oxidation reaction than NC-T- and carbon black-supported Pt-Sn catalysts [41]. Wang et al. [42] found that MOF-derived CeO_2-supported Ag catalysts (Ag-Ce-BTC-C) prepared via one-pot and pyrolysis at 500 °C under Ar and O_2 atmosphere displayed good catalytic performance for the toluene oxidation reaction (T_{90} = 226 °C).

Among the various types of MOFs, Zr-based MOFs have been extensively studied by catalysis scholars owing to the strong Zr-O coordination bond, feasible synthesis conditions, and the ease of reproducibility [43,44]. UiO-67 is one of the Zr-MOFs, which consists of $Zr_6(OH)_4O_4$ clusters and 4,4-biphenyl dicarboxylic acid (H_2bpdc) linkers [45,46]. In the present study, a series of UiO-67-CTAB(n) (CTAB: cetyltrimethylammonium bromide; n: the concentration of CTAB; *n* = 0, 3, 8, 13, 18) with different physicochemical properties (crystal morphology, crystal size, BET specific surface area, etc.) were prepared by the surfactant CTAB assistant solvothermal method. PdNi/UiO-67-CTAB(n)-A500 catalysts were obtained by co-impregnation and pyrolysis at 500 °C under air atmosphere using UiO-67-CTAB(n) as a sacrificial template. The effect of various factors such as the physicochemical property of the MOF template, reaction temperature, and reaction time on the hydrogenation of 1,3-butadiene was studied. A 1,3-butadiene hydrogenation test found that PdNi/UiO-67-CTAB(3)-A500 presented the best catalytic performance for 1,3-butadiene hydrogenation. The recoverability and reusability of the PdNi/UiO-67-CTAB(3)-A500 catalyst were also investigated.

2. Results and Discussion

2.1. Synthesis and Characterization

The synthesis procedure was illustrated in a schematic representation (Scheme 1). UiO-67-CTAB(n) (*n* = 0, 3, 8, 13, 18) was simply synthesized from $ZrCl_4$, H_2bpdc, acetic

acid, CTAB, and DMF by the surfactant CTAB assistant solvothermal method using different CTAB concentrations. Then, the PdNi/UiO-67-CTAB(n)-A500 (n = 0, 3, 8, 13, 18) catalyst was synthesized by the co-impregnation and pyrolysis method using $PdCl_2$ and $Ni(NO_3)_2{\cdot}6H_2O$ as the metal precursor.

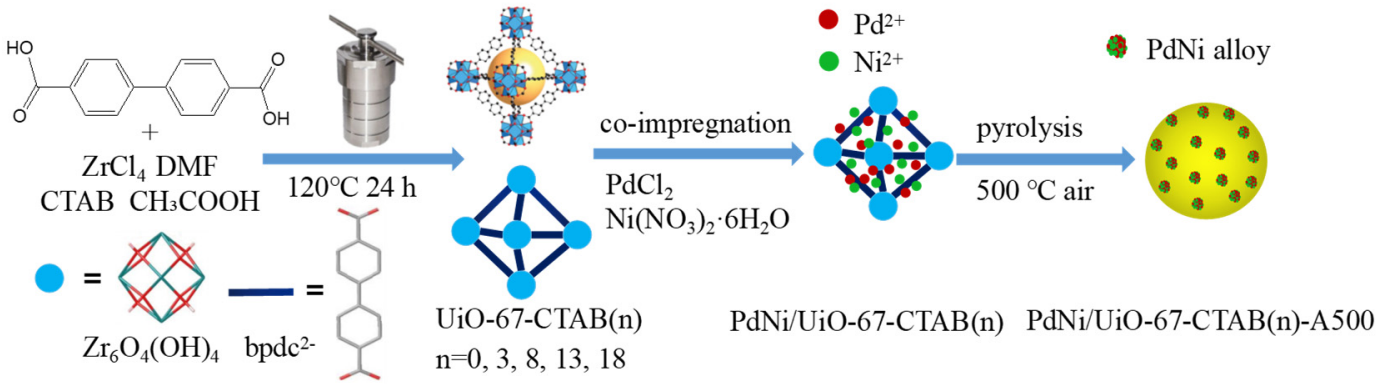

Scheme 1. Schematic illustration of PdNi/UiO-67-CTAB(n)-A500 (n = 0, 3, 8, 13, 18) catalysts.

Viewing SEM images, the crystal morphology of UiO-67-CTAB(0) contains both regular octahedral crystals and irregular polyhedral crystals, and it shows a broad crystal size, which ranged from 200 to 2800 nm as a result of the high-degree intergrowth and aggregation of primary crystals (Figure 1) [47]. After adding CTAB to the synthesis solution, UiO-67-CTAB(3) exhibited a uniform octahedral morphology with a crystal size of ca. 1500 nm, which was consistent with the morphology of UiO-67 reported in the literature [48,49]. During the process of crystallization, CTAB was adsorbed on the surface of the UiO-67 primary crystal, which would decrease the van der Waals force and surface energy, promoting the ordered agglomeration, thus forming a more regular morphology [50–52]. The long hydrocarbon chains of CTAB also repelled each other, preventing the further interaction with other UiO-67 crystals and excessive growth of UiO-67, resulting in a smaller particle size [53,54]. However, further increasing the concentration of CTAB in the synthetic solution, irregular polyhedral crystals appeared in the synthesized crystals. The percent of irregular polyhedral crystals increased with the increase in CTAB concentration, up to about 100% when the CTAB concentration was 18 g/L. The crystal particle sizes of UiO-67-CTAB(8), UiO-67-CTAB(13), and UiO-67-CTAB(18) were ca. 1100 nm, 2300 nm, and 300 nm, respectively. The concentration of CTAB in synthetic mixture also had a significant effect on the particle size, and the crystal size was varied as follows: UiO-67-CTAB(13) > UiO-67-CTAB(3) > UiO-67-CTAB(8) >UiO-67-CTAB(18) > UiO-67-CTAB(0). These results indicated that excessive CTAB has a negative effect on the formation of a uniform morphology. This may be owing to the fact that most CTAB existed as micelles, rather than dispersed forms, which did not interact well with surfaces [51,55]. Wang et al. [52] also reported that the morphology and size of 146S@ZIF-8 can be changed by adding CTAB. Jubeer et al. [56] reported that the particle size of ZnS could be adjusted by changing the concentration of CTAB. Ping et al. [57] found that NiPO was of a flake shape at a low CTAB:P molar ratio, and the samples began to appear with a tubular structure with the increase in the CTAB:P molar ratio.

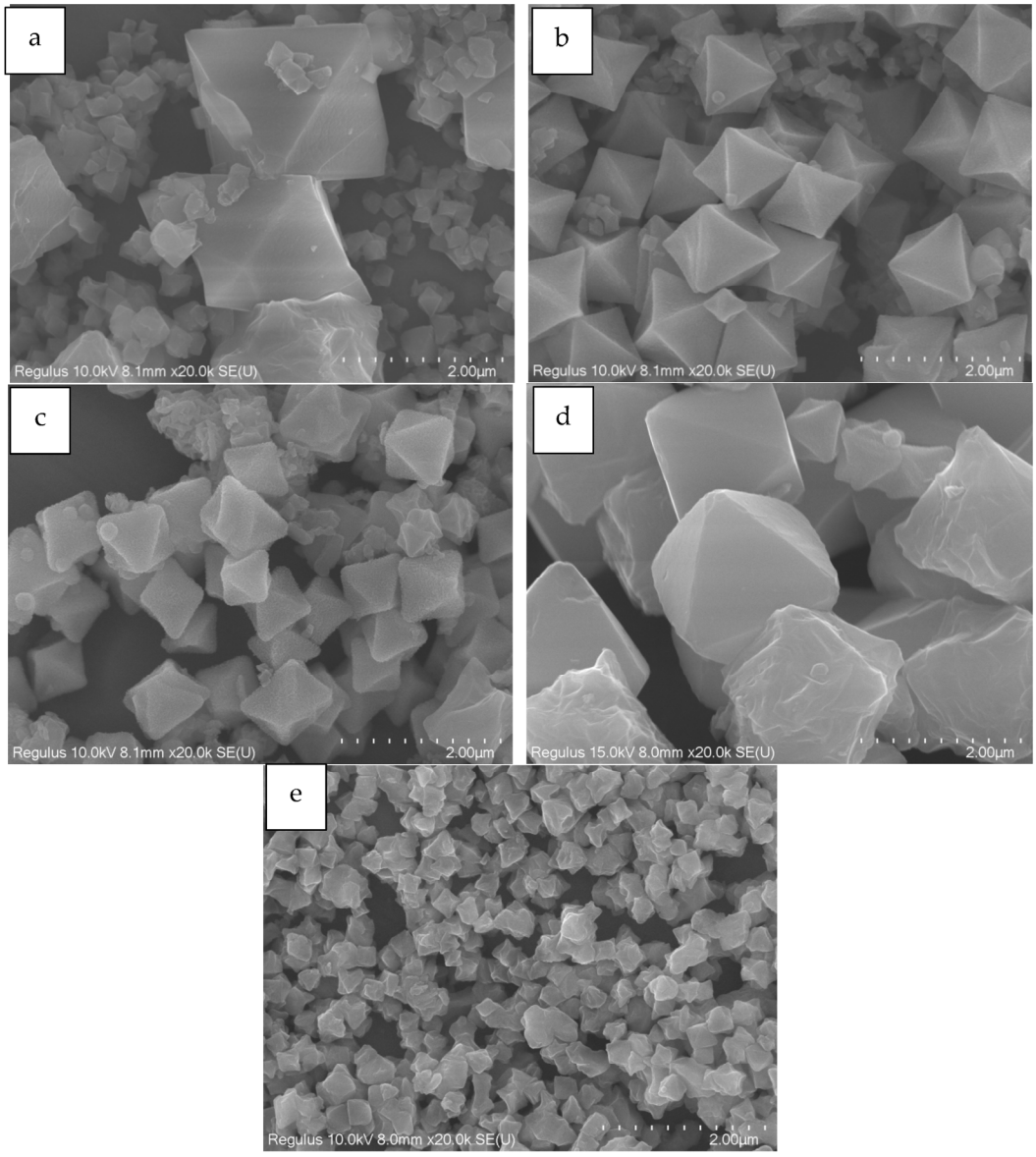

Figure 1. SEM photographs of UiO-67-CTAB(0) (**a**), UiO-67-CTAB(3) (**b**), UiO-67-CTAB(8) (**c**), UiO-67-CTAB(13) (**d**), and UiO-67-CTAB(18) (**e**).

The TEM images and Pd–Ni nanoparticle size distribution histograms of PdNi/UiO-67-CTAB(n)-A500 (n = 0, 3, 8, 13, 18) catalysts are displayed in Figure S1. As shown in Figure S1, the PdNi/UiO-67-CTAB(0)-A500, PdNi/UiO-67-CTAB(3)-A500, and PdNi/UiO-67-CTAB(18)-A500 catalysts had a narrow nanoparticle size distribution with an average particle size of 6.0, 6.7, and 6.0 nm, respectively. However, PdNi/UiO-67-CTAB(8)-A500 and PdNi/UiO-67-CTAB(13)-A500 showed broader nanoparticle size distribution with an average particle size of 15.3 and 9.2 nm. The characterization of the catalysts by TEM displayed that PdNi/UiO-67-CTAB(8)-A500 presented the largest average particle size, PdNi/UiO-67-CTAB(13)-A500 presented the middle average particle size, and the PdNi/UiO-67-CTAB(0)-A500, PdNi/UiO-67-CTAB(3)-A500, and PdNi/UiO-67-CTAB(18)-A500 catalysts presented smaller average particles sizes. The HAADF-STEM and EDS mapping of the PdNi/UiO-67-CTAB(3)-A500 catalyst are displayed in Figure 2. The HAADF-STEM and EDS mapping of PdNi/UiO-67-CTAB(3)-A500 demonstrated that Pd and Ni elements were highly intermixed and evenly distributed on the support, confirming the formation of Pd-Ni alloys [58,59].

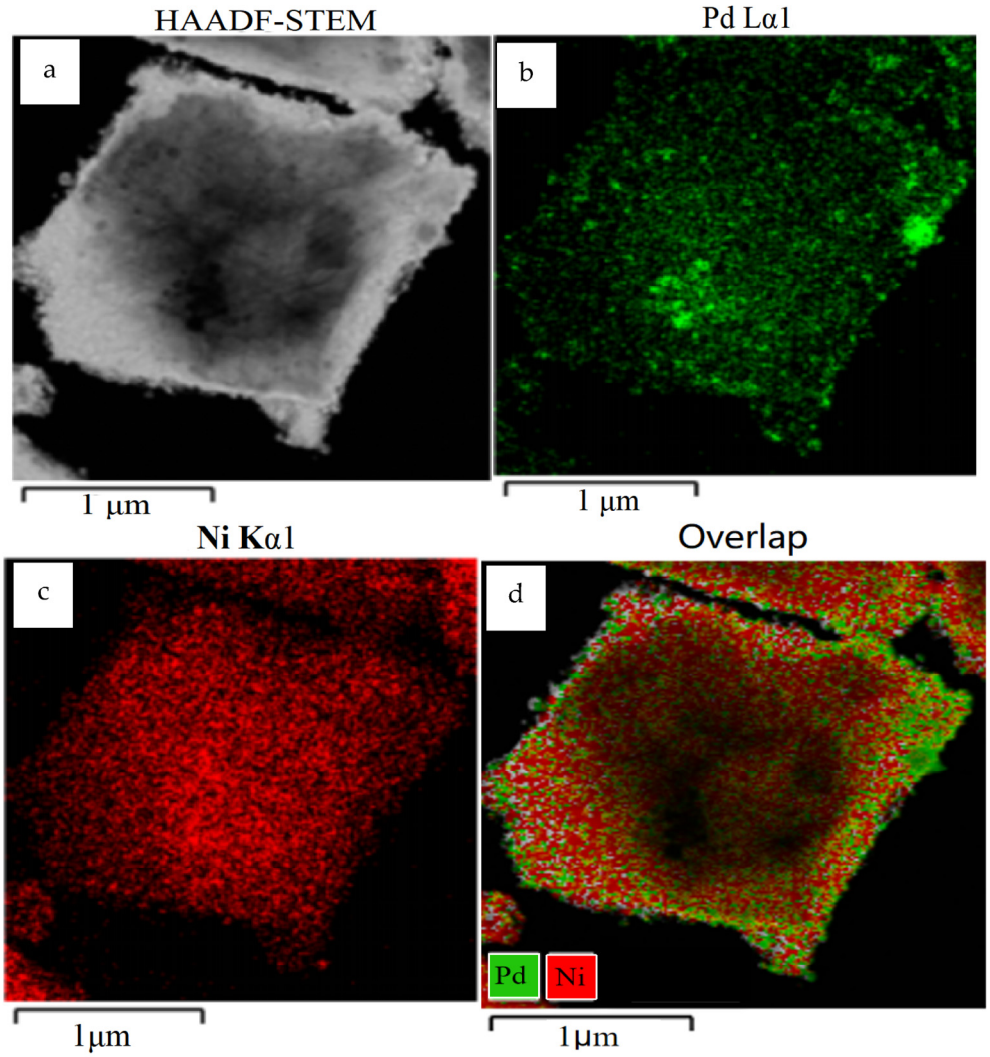

Figure 2. HAADF-STEM (**a**) and EDS mappings (**b**–**d**) of PdNi/UiO-67-CTAB(3)-A500.

The samples of UiO-67-CTAB(n) and PdNi/UiO-67-CTAB(n)-A500 (n = 0, 3, 8, 13, 18) have been characterized by PXRD. The PXRD patterns of UiO-67-CTAB(n) and PdNi/UiO-67-CTAB(n)-A500 (n = 0, 3, 8, 13, 18) are presented in Figure 3. PXRD analysis displayed that all the 2θ peaks of UiO-67-CTAB(0) corresponded well with UiO-67 reported in the literature, illustrating that UiO-67-CTAB(0) has been successfully synthesized [44,60,61]. The PXRD peaks of the synthesized UiO-67-CTAB(3), UiO-67-CTAB(8), UiO-67-CTAB(13), and UiO-67-CTAB(18) were almost identical to UiO-67-CTAB(0), which indicates that the synthesized samples had the original UiO-67-CTAB(0) structure (Figure 3a). However, the PXRD peak intensity of UiO-67-CTAB(18) decreased significantly, revealing that its crystallinity was significantly lost (Figure 3a). After pyrolysis at 500 °C under air, the PXRD patterns changed completely (Figure 3b). There was no characteristic diffraction peak from UiO-67 for the PdNi/UiO-67-CTAB(n)-A500 (n = 0, 3, 8, 13, 18) catalysts, indicating that UiO-67 was completely decomposed [62]. The PdNi/UiO-67-CTAB(n)-A500 (n = 0, 3, 8, 13, 18) catalysts all exhibited four diffraction peaks at 2θ values of 30.15, 33.84, 50.57, and 60.30° which could be assigned to the (111), (200), (220), and (311) crystallographic planes of tetragonal ZrO_2 (t-ZrO_2), respectively [44,62–66]. However, the characteristic PXRD diffraction peaks of the PdNi alloy were not detected in PdNi/UiO-67-CTAB(n)-A500 (n = 0, 3, 8, 13, 18) due to the low amounts of Pd and Ni and the high dispersion of PdNi alloy nanoparticles on the UiO-67-CTAB(n) (n = 0, 3, 8, 13, 18) supports [67,68].

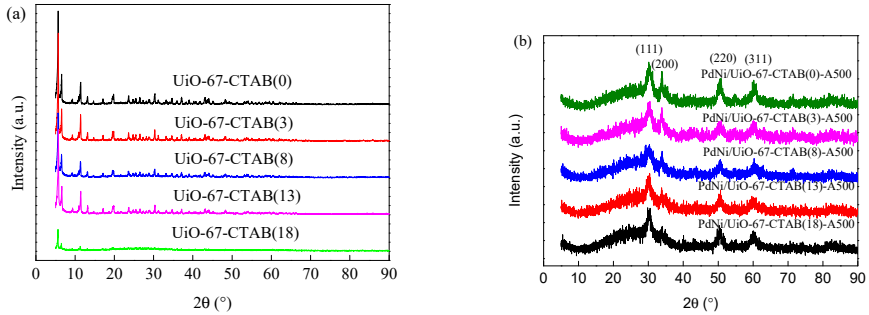

Figure 3. PXRD patterns of UiO-67-CTAB(n) (**a**) and PdNi/UiO-67-CTAB(n)-A500 (**b**) (n = 0, 3, 8, 13, 18).

UiO-67-CTAB(n) and PdNi/UiO-67-CTAB(n)-A500 (n = 0, 3, 8, 13, 18) have been characterized by nitrogen adsorption–desorption at 77 K to estimate the specific surface area, porosity volume, and pore diameter. The specific areas and pore size distributions were determined using the Brunauer–Emmett–Teller (BET) method and density functional theory (DFT) method, respectively [69]. The nitrogen sorption isotherms and pore size distribution diagrams are displayed in Figure 4, and the BET surface area and pore volume dates are displayed in Table 1. As shown in Figure 4a, UiO-67-CTAB(n) (n = 0, 3, 8, 13, 18) displayed a pronounced type-I isotherm, indicating the existence of micropores [44]. The DFT-computed pore size distributions displayed maximum values at 0.82 and 1.27 nm for UiO-67-CTAB(0) (Figure 4b). The pore diameters determined by the DFT method were 1.05, 1.09, 1.09, and 1.09 nm for UiO-67-CTAB(3), UiO-67-CTAB(8), UiO-67-CTAB(13), and UiO-67-CTAB(18), respectively (Figure 4b). However, PdNi/UiO-67-CTAB(n)-A500 (n = 0, 3, 8, 13, 18) displayed a type-IV isotherm, indicating the emergence of a mesoporous structure after the loading of Pd-Ni nanoparticles and pyrolysis at 500 °C (Figure 4c) [70,71]. The pore diameters based on the BJH model were 3.57, 3.59, 3.53, 3.58, and 3.54 nm for PdNi/UiO-67-CTAB(0)-A500, PdNi/UiO-67-CTAB(3)-A500, PdNi/UiO-67-CTAB(8)-A500, PdNi/UiO-67-CTAB(13)-A500, and PdNi/UiO-67-CTAB(18)-A500, respectively (Figure 4d). The BET surface areas were 686.1, 264.9, 1402.2, 1611.8, and 1309.1 m^2/g for UiO-67-CTAB(0), UiO-67-CTAB(3), UiO-67-CTAB(8), UiO-67-CTAB(13), and UiO-67-CTAB(18), respectively (Table 1). The total pore volumes were 0.4, 0.17, 0.73, 0.83, and 0.70 cm^3/g for UiO-67-CTAB(0), UiO-67-CTAB(3), UiO-67-CTAB(8), UiO-67-CTAB(13), and UiO-67-CTAB(18), respectively (Table 1). The BET surface areas and pore volumes were varied as follows: UiO-67-CTAB(13) > UiO-67-CTAB(8) > UiO-67-CTAB(18) > UiO-67-CTAB(0) > UiO-67-CTAB(3). As shown in SEM, the crystal size showed the order UiO-67-CTAB(13) > UiO-67-CTAB(3) > UiO-67-CTAB(8) > UiO-67-CTAB(18) > UiO-67-CTAB(0) (Figure 1). UiO-67-CTAB(3) exhibited a uniform octahedral morphology, and the percent of irregular polyhedral crystals increased with the increase in CTAB concentration. The above results indicated that the BET surface area and pore volume were not only affected by the regularity of the morphology but also by the crystal size. Osuga et al. [72] reported that the BET surface area and pore volume were greatly affected by the morphology of aluminosilicate zeolites. The formation of sheet-like particles increased the BET surface area and decreased the micropore volume [72]. Li et al. [73] found that the different BET surface area of 2D metal–organic frameworks CuBDC (BDC: 1,4-benzenedicarboxylic) and CuBDC-NBA (NBA:4-n-butylbenzoic acid) were induced by their different morphology and size. The BET surface areas and pore volumes of PdNi/UiO-67-CTAB(n)-A500 (n = 0, 3, 8, 13, 18) catalysts after Pd-Ni nanoparticle loading and pyrolysis at 500 °C decreased significantly compared to UiO-67-CTAB(n) (n = 0, 3, 8, 13, 18). This may be due to the fact that UiO-67 completely decomposed and formed t-ZrO_2. The PdNi/UiO-67-CTAB(n)-A500 (n = 0, 3, 8, 13, 18) catalysts displayed a similar BET surface area (54.3–66.7 m^2/g) and pore volumes (0.09–0.11 cm^3/g), illustrating that the properties (BET surface area, pore diameter, and pore volume) of the MOF template have little influence on the BET surface area and pore volume of the catalysts obtained by pyrolysis.

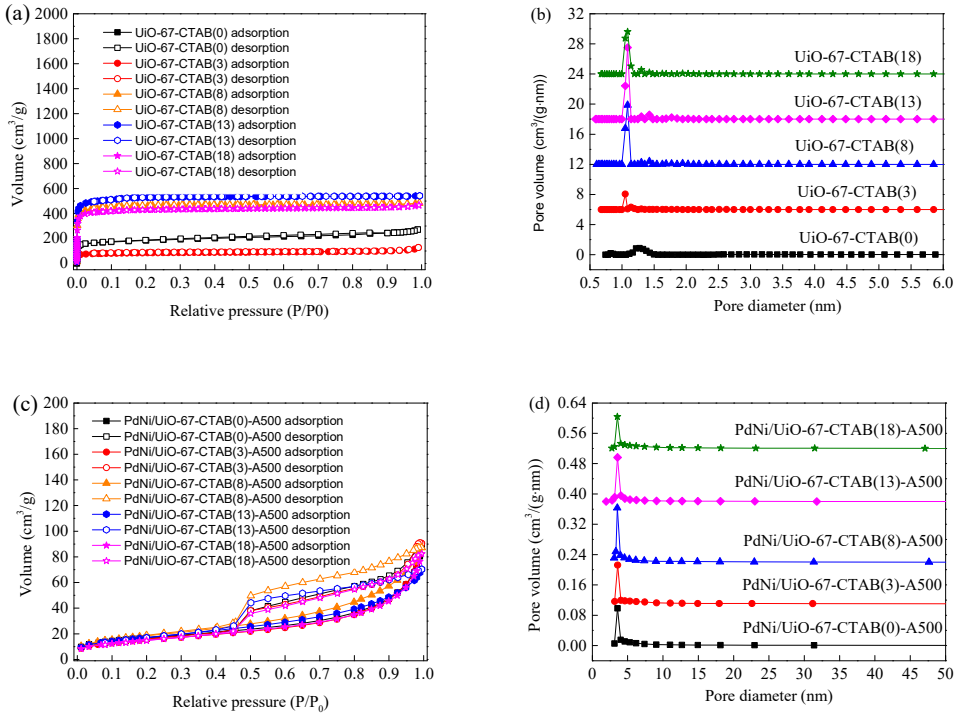

Figure 4. (**a**) N_2-sorption isotherms of UiO-67-CTAB(n) (n = 0, 3, 8, 13, 18); (**b**) pore diameter distributions of UiO-67-CTAB(n) (n = 0, 3, 8, 13, 18) calculated using DFT method; (**c**) N_2-sorption isotherms of PdNi/UiO-67-CTAB(n)-A500 (n = 0, 3, 8, 13, 18); (**d**) pore diameter distributions of PdNi/UiO-67-CTAB(n)-A500 (n = 0, 3, 8, 13, 18) calculated using DFT method.

Table 1. Comparison of physicochemical properties of different samples.

Entry	Sample	S_{BET} (m^2/g)	V_{total} (cm^3/g)
1	UiO-67-CTAB(0)	686.1	0.40
2	UiO-67-CTAB(3)	264.9	0.17
3	UiO-67-CTAB(8)	1402.2	0.73
4	UiO-67-CTAB(13)	1611.8	0.83
5	UiO-67-CTAB(18)	1309.1	0.70
6	PdNi/UiO-67-CTAB(0)-A500	60.9	0.09
7	PdNi/UiO-67-CTAB(3)-A500	54.6	0.09
8	PdNi/UiO-67-CTAB(8)-A500	66.7	0.11
9	PdNi/UiO-67-CTAB(13)-A500	62.4	0.09
10	PdNi/UiO-67-CTAB(18)-A500	54.3	0.09

The elemental composition and chemical valence state of the PdNi/UiO-67-CTAB(3)-A500 catalyst were studied by XPS. Figure 5 presents the full XPS spectra along with the Pd 3d, Ni 3p, and C1s narrow scan spectra of PdNi/UiO-67-CTAB(3)-A500. It can be seen in the full survey scan spectra that the PdNi/UiO-67-CTAB(3)-A500 catalyst was mainly composed of Pd, Ni, Zr, O, and C (Figure 5a). The Pd 3d spectrum of PdNi/UiO-67-CTAB(3)-A500 can be deconvoluted into four peaks; the binding energies at 332.7 and 342.5 eV can be ascribed to Pd^0 $3d_{5/2}$ and Pd^0 $3d_{3/2}$, whereas the two peaks at 337.1 and 346.2 eV can be ascribed to Pd^{2+} $3d_{5/2}$ and Pd^{2+} $3d_{3/2}$ (Figure 5b) [20,74]. For the Ni 3p spectrum of PdNi/UiO-67-CTAB(3)-A500, a peak at 855.3 eV as well as a satellite peak at 861.4 eV were apparent in the Ni^{2+} $2p_{3/2}$ region, whereas a signal at 873.1 eV as well as a satellite peak at 879.6 eV were observed in the Ni^{2+} $2p_{5/2}$ region (Figure 5c) [34,75]. As shown in C1s peaks, the strong peak at 284.4 eV was attributed to the graphite carbon, and the peaks at 284.8 eV, 286.4 eV, and 288.7 eV corresponded to the calibration peak C–C, C–O–C, and O = C–O, respectively (Figure 5d) [76,77]. The Raman spectra of PdNi/UiO-

67-CTAB(3)-A500 displayed two obvious peaks at 1381 cm^{-1} (D band) and 1592 cm^{-1} (G band) which can be attributed to the amorphous carbon species and highly symmetrical and ordered graphitized carbon species (Figure 6) [78,79]. Both the results of XPS and Raman spectroscopy for PdNi/UiO-67-CTAB(3)-A500 illustrated the existence of carbon species; this may be due to the incomplete combustion of catalysts.

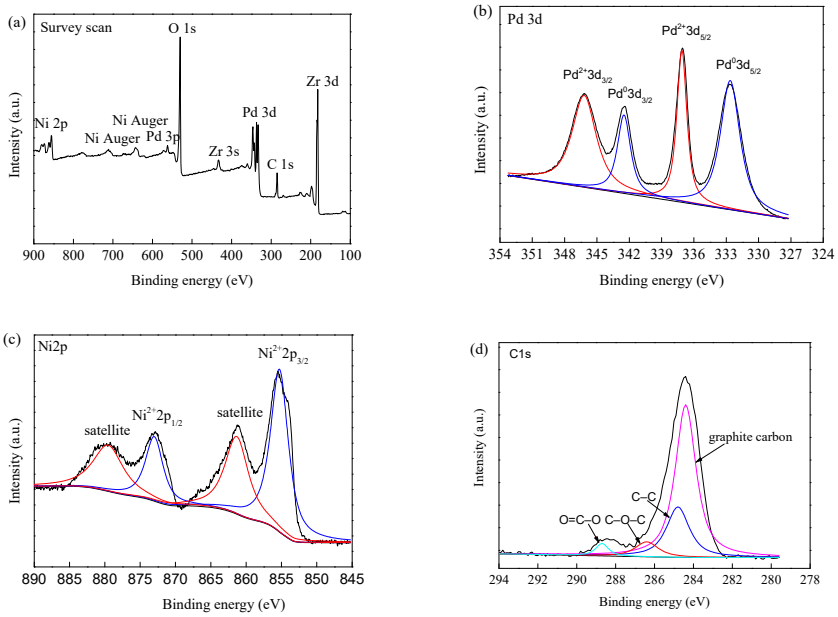

Figure 5. XPS spectra of survey scan (**a**), Pd 3d (**b**), Ni 2p (**c**), and C1s (**d**) for PdNi/UiO-67-CTAB(3)-A500.

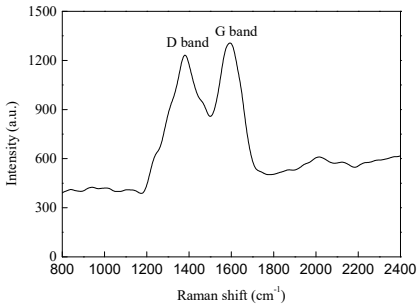

Figure 6. Raman spectra of PdNi/UiO-67-CTAB(3)-A500.

2.2. Catalytic Performance and Stability

The catalytic performance of PdNi/UiO-67-CTAB(n)-A500 (n = 0, 3, 8, 13, 18) for the hydrogenation of 1,3-butadiene was investigated. The hydrogenation activity of the blank (without catalyst) can be neglected owing to the low 1,3-butadiene conversion (<1%) at 25–40 °C. Figure 7 exhibits the 1,3-butadiene conversion and product selectivity of PdNi/UiO-67-CTAB(3)-A500 at different reaction temperatures (25–40 °C). At a low temperature of 25 °C, the conversion of 1,3-butadiene first increased, then decreased, and thereafter remained constant with the extension of the reaction time (Figure 7a). The initial conversion of 1,3-butadiene was only 4.7%; yet when the reaction time was 1 h, the conversion reached the maximum, up to 46.0%; the conversion was 34.2% within 6 h (Figure 7a). At a temperature of 30 °C, the conversion of 1,3-butadiene first increased and then decreased with values ranging from 71.3% to 96.1% (Figure 7a). At a relatively high reaction temperature of 40 °C, the conversion of 1,3-butadiene decreased with an increase in reaction time, and the conversions decreased from 99.9% to 85.4% (Figure 7a). The results displayed that the increase in the reaction temperature resulted in a continuous increase in 1,3-butadiene conversion. The ideal products of 1,3-butadiene hydrogenation were butenes

(including 1-butene, *trans*-2-butene, and *cis*-2-butene), and butenes can be converted into butane by further hydrogenation [23,45]. The butane (44.2–49.0%) and total butene (51.0–55.8%) selectivities over PdNi/UiO-67-CTAB(3)-A500 changed slightly with the increase in reaction time at 25 °C (Figure 7b). The selectivity of *trans*-2-butene increased during the first 1 h of the reaction, then decreased from 1 h to 4 h, and then remained essentially constant from 4 h to 6 h (Figure 7b). However, the selectivity toward 1-butene displayed an opposite tendency compared to *trans*-2-butene over the entire reaction time range (Figure 7b). The selectivity of *cis*-2-butene remained approximately constant throughout the whole reaction time range, ranging from 6.8% to 8.9% (Figure 7b). When the reaction temperature rose to 30 °C, there was very little change in the distribution of products in the order of butane (47.3–52.3%) > 1-butene (22.7–27.9%) > *trans*-2-butene (15.7–18.3%) > *cis*-2-butene (7.0–8.0%) (Figure 7c). When the reaction temperature was further increased to 40 °C, the product distribution changed in the order of butane (54.3–56.7%) > *trans*-2-butene (20.3–22.3%) > 1-butene (15.0–18.1%) > *cis*-2-butene (6.1–6.7%) (Figure 7d). When the reaction temperature increased from 25 °C to 40 °C, the selectivity toward total butenes slightly decreased from 51.0–55.8% to 43.5–45.7%, and the selectivity toward butane increased from 44.2–49.0% to 54.3–56.5% (Figure 7). This may be due to the stronger adsorption of butenes that was generated on surface PdNi alloy nanoparticles at a higher temperature, resulting in deep hydrogenation [80,81]. Therefore, the higher reaction temperature promotes the secondary hydrogenation of butenes to butane [59]. The data of Figure 7 proved that the 1,3-butadiene conversion and selectivity of PdNi/UiO-67-CTAB(3)-A500 were related to the reaction temperature; as the reaction temperature increased, the 1,3-butadiene conversion of the catalyst increased, and the selectivity toward total butenes decreased.

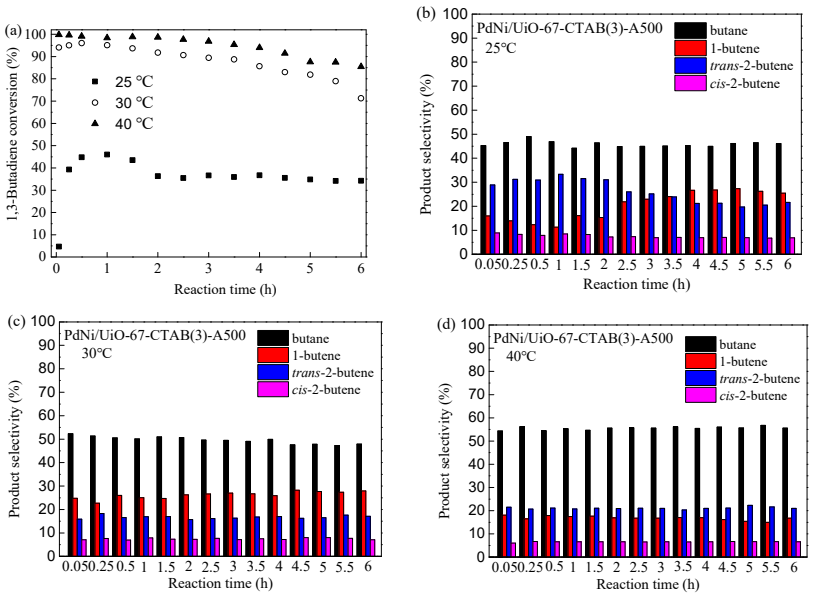

Figure 7. 1,3-butadiene conversion profiles (**a**) and product selectivity histograms (**b**–**d**) over PdNi/UiO-67-CTAB(3)-A500 catalyst at different reaction temperatures (25–40 °C) (reaction conditions: 20 mL/min 1.0 vol% 1,3-butadiene balanced with N_2, 10 mL/min 99.999% H_2, catalyst quantity = 5 mg).

The 1,3-butadiene conversions and product selectivities of PdNi/UiO-67-CTAB(n)-A500 (n = 0, 3, 8, 13, 18) catalysts for the selective hydrogenation of 1,3-butadiene are shown in Figure 8. Clearly, PdNi/UiO-67-CTAB(3)-A500 displayed the best performance for the selective hydrogenation of 1,3-butadiene. For the PdNi/UiO-67-CTAB(3)-A500 catalyst, the 1,3-butadiene conversion was maintained at about 99.0% at the first 2 h of the reaction, then gradually decreased as the reaction proceeded further, and the conversion of 1,3-butadiene dropped to 85.4% within 6 h (Figure 8a). The selectivity to total butenes changed slightly in the whole reaction process, and its value was between 43.5% and 45.7%

(Figure 8c). For the PdNi/UiO-67-CTAB(0)-A500 catalyst, the conversion of 1,3-butadiene slightly increased during the first 0.25 h and then decreased significantly from 0.5 h to 6 h (Figure 8a). The selectivity of total butenes decreased during the first 0.25 h and then increased from 0.5 h to 6 h (Figure 8b). The conversion of 1,3-butadiene and the selectivity of total butenes were 67.6% and 66.9% after reaction 6 h at 40 °C for PdNi/UiO-67-CTAB(0)-A500, respectively (Figure 8a,b). The PdNi/UiO-67-CTAB(13)-A500 catalyst displayed a similar shaped conversion curve and catalytic performance to that of the PdNi/UiO-67-CTAB(0)-A500 catalyst (Figure 8a,e). The 1,3-butadiene conversion and selectivity to total butenes were 66.5% and 63.2% within 6 h at 40 °C for the PdNi/UiO-67-CTAB(13)-A500 catalyst, respectively (Figure 8a,e). For the PdNi/UiO-67-CTAB(8)-A500 catalyst, the 1,3-butadiene conversion slightly increased during the first 0.25 h of the reaction, leveling off from 0.5 h to 3.5 h, and slightly decreased from 4 h to 6 h (Figure 8a). The selectivity for total butenes changed slightly at all reaction times, with values ranging from 41.8% to 47.1% (Figure 8d). The PdNi/UiO-67-CTAB(18)-A500 catalyst displayed the lowest catalytic activity. 1,3-butadiene was slightly increased with reaction time during the first 0.5 h varying from 44.2% to 51.3% and slightly decreased from 1 h to 6 h (42.0–46.6%) (Figure 8a). The selectivity of total butenes ranged from 48.2% to 59.3% for the PdNi/UiO-67-CTAB(18)-A500 catalyst (Figure 8f). These results indicated that the crystal size, BET surface area, and pore volume of the UiO-67 template have little effect on the catalytic activity of the catalyst. However, the crystal morphology of the UiO-67 template has an important effect on the catalytic activity of the catalyst. The PdNi/UiO-67-CTAB(3)-A500 catalyst which was synthesized using UiO-67-CTAB(3) with uniform octahedral morphology as a template displayed the highest catalytic activity, while that of PdNi/UiO-67-CTAB(18)-A500 with 100% irregular polyhedral crystals was the worst.

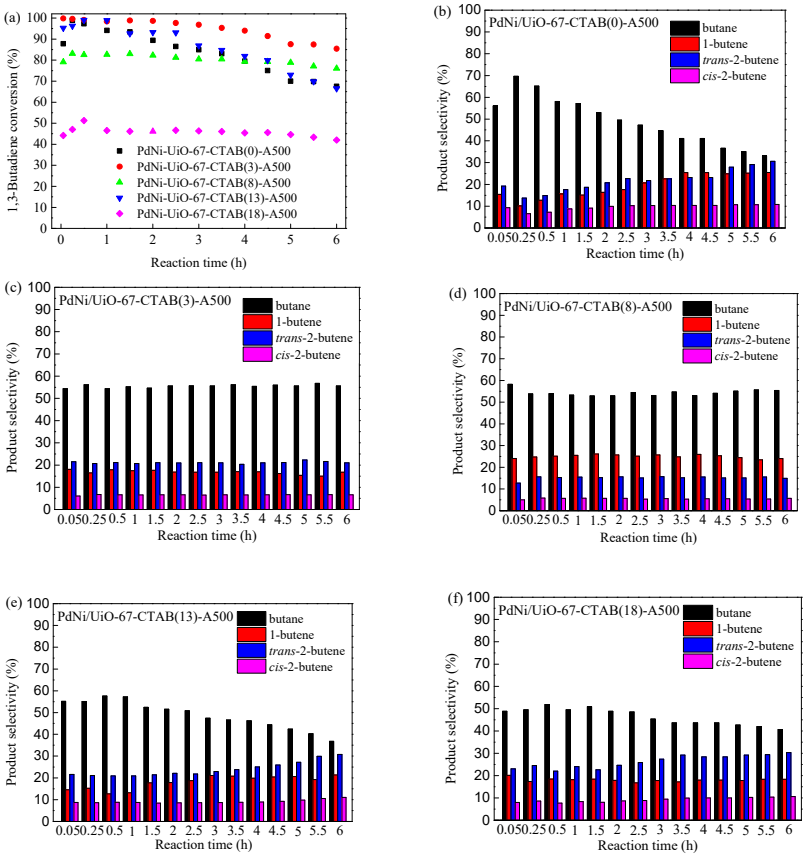

Figure 8. 1,3-butadiene conversion profiles (**a**) and product selectivity histograms (**b**–**f**) over PdNi/UiO-67-CTAB(n)-A500 (n = 0, 3, 8, 13, 18) catalysts at 40 °C (reaction conditions: 20 mL/min 1.0 vol% 1,3-butadiene balanced with N_2, 10 mL/min 99.999% H_2, catalyst quantity = 5 mg).

A brief comparison of the catalytic performance of reported Pd-based catalysts for the hydrogenation of 1,3-butadiene is presented in Table 2. It can be seen that our prepared PdNi/UiO-67-CTAB(3)-A500 catalyst displayed excellent 1,3-butadiene hydrogenation performance as compared to the reported hydrogenation monometallic Pd catalysts (Table 2, entries 1–4) [9,82]. The addition of Ni to a Pd monometallic catalyst can change the structure and electronic properties of the Pd catalyst and improve 1,3-butadiene conversion and butene selectivity [18,19]. The PdNi/UiO-67-CTAB(3)-A500 catalyst displayed better hydrogenation activity than SiO_2- and UiO-66-NH_2-supported Pd-Ni bimetallic catalysts (Table 2, entries 1, 6, 11) [13,20]. However, our prepared catalyst PdNi/UiO-67-CTAB(3)-A500 displayed lower hydrogenation activity than Ni_1-Pd_1/ZnO, single-atom Au@Pd@SiO_2, Pd–Cu/Mn_2O_3, and PdNi/UiO-66 (1:1) catalysts (Table 2, entries 1, 5, 8–10) [13,20,83,84]. Although our prepared PdNi/UiO-67-CTAB(3)-A500 catalyst exhibited higher 1,3-butadiene conversion than that of the Pd-Ag/ES catalyst for the hydrogenation of 1,3-butadiene, its selectivity for total butenes was lower (Table 2, entries 1, 7) [24].

Table 2. The catalytic performance of reported Pd-based catalysts in the hydrogenation of 1,3-butadiene.

Entry	Catalyst	Pd Loading (wt%)	Pd Size (nm)	T (°C)	Conv. (%)	Sel. (%)	Ref.
1	PdNi/UiO-67-CTAB(3)-A500	6.5	6.7	40	98.4	44.8	this work
2	Pd/pollen-C-500	1	112.6	50	23.0	97.9	9
3	1PdGONE	1	8.9	50	15	88	82
4	2PdG	2	4.9	50	89	27	82
5	Ni_1-Pd_1/ZnO	-	3.6	35	98.8	90.0	13
6	Ni_1-Pd_1/SiO_2	-	3.2	35	44.0	93.8	13
7	Pd-Ag/ES	0.5	3.7	45	95.0	95.8	24
8	Au@Pd@SiO_2	0.02	monodisperse	35	98.0	80.0	83
9	Pd–Cu/Mn_2O_3	1	3.8	50	99.1	92.0	84
10	PdNi/UiO-66 (1:1)	2.65	7.1	40	99.8	84.5	20
11	PdNi/UiO-66-NH_2 (1:1)	2.51	4.6	40	15.6	99.5	20

The stability of catalysts is an important factor to be considered in industrial production [18,85]. Stability testing is highly necessary for the promotion and actual production of the catalyst. The durability of the PdNi/UiO-67-CTAB(3)-A500 catalyst was first examined for 60 h at 40 °C. Then, the catalyst was regenerated in N_2 (12 mL/min) flowing at 200 °C for 1 h and tested for another 30 h. As shown in Figure 8a, PdNi/UiO-67-CTAB(3)-A500 was significantly deactivated during a total 60 h of the reaction time on the stream; the 1,3-butadiene conversion decreased from 99.9% to 27.6%. However, the product selectivity changed slightly at all reaction times (Figure 9b). The selectivity of total butenes varied between 43.6% and 45.7%. The regenerated PdNi/UiO-67-CTAB(3)-A500 catalyst displayed improved catalytic activity (Figure 9a). The conversion of 1,3-butadiene reached 85.5% after PdNi/UiO-67-CTAB(3)-A500 regenerated in flowing N_2 at 200 °C for 1 h and then gradually decreased over the next 30 h. The total butene selectivity of the regenerated PdNi/UiO-67-CTAB(3)-A500 catalyst increased gradually at the first 18 h and then leveled off with the reaction. These results showed that the catalyst of PdNi/UiO-67-CTAB(3)-A500 can be regenerated at 200 °C. It was previously reported that carbon will be produced during the process of 1,3-butadiene hydrogenation, and the accumulation carbon will block the catalyst channels or deposit on the catalyst as films, thus leading to the deactivation of the catalyst [59,78,86,87]. The PdNi/UiO-67-CTAB(3)-A500 catalyst after the reaction at 40 °C for 24 h on the stream was characterized by TG in air atmosphere to analyze the deposited carbon. From the TG curve in Figure 10, the first weight loss stage from 30 °C to 275 °C owed to the release of physically adsorbed raw materials (1,3-butadiene and H_2) and product materials (butane, 1-butene, *trans*-2-butene, and *cis*-2-butene). XPS displayed that Pd in PdNi/UiO-67-CTAB(3)-A500 existed as Pd^0 and Pd^{2+} (Figure 5b). The TG curves showed a slight increase (1%) in weight from 275 °C to 700 °C, illustrating that Pd^0 started to oxidize. Then, the TG curve had a decrease with the weight loss of 1.7% from 730 °C to

910 °C due to the deposited carbon being oxidized to generate CO_2 and CO gases [88]. The calculated deposition carbon rate was 0.71 mg/(h·g_{cat}).

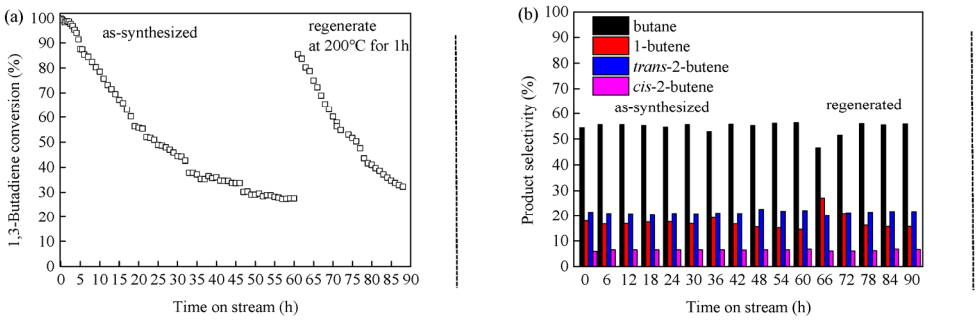

Figure 9. Stability and regenerate test of PdNi/UiO-67-CTAB(3)-A500 catalyst: (**a**) conversion; (**b**) product selectivity (reaction conditions: 20 mL/min 1.0 vol% 1,3-butadiene balanced with N_2, 10 mL/min 99.999% H_2, catalyst quantity = 5 mg, 40 °C).

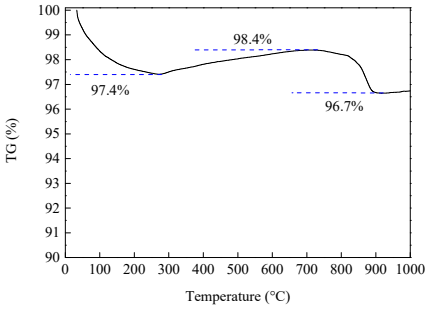

Figure 10. TG-DTA of PdNi/UiO-67-CTAB(3)-A500 after reaction at 40 °C for 24 h on stream.

3. Experimental Section

3.1. Synthesis of UiO-67-CTAB

UiO-67-CTAB(n) (n = 0, 3, 8, 13, 18) was prepared by using the surfactant CTAB assistant solvothermal method (CTAB: cetyltrimethylammonium bromide). First, $ZrCl_4$ (0.64 mmol, 150.00 mg), 4,4-biphenyldicarboxylic acid (H_2bpdc, 0.72 mmol, 175.00 mg), acetic acid (5 mL), and surfactant CTAB (0.135 g) were dissolved in 40 mL *N*,*N*′-dimethylformamide (DMF). Subsequently, the mixture was transferred into a 100 mL Teflon-lined autoclave reactor and maintained at 120 °C in a drying oven for 24 h. After natural cooling to room temperature, the white slurry was centrifuged. The obtained white solid was then washed three times with DMF and anhydrous methanol, respectively. Finally, the remaining white solid was dried under vacuum (vacuum degree: 0.1 MPa) at 50 °C for 5 h. The resultant powder was named as UiO-67-CTAB(3). The UiO-67-CTAB(8), UiO-67-CTAB(13), and UiO-67-CTAB(18) samples were synthesized by using a similar procedure, except using different CTAB concentrations (8, 13, and 18 g/L). The sample also synthesized by using a similar method without CTAB was named as UiO-67-CTAB(0) as the control.

3.2. Synthesis of PdNi/UiO-67-CTAB-A500

The PdNi/UiO-67-CTAB(n)-A500 (n: the concentration of CTAB; n = 0, 3, 8, 13, 18; A500: pyrolysis at 500 °C under an air atmosphere) catalyst was synthesized by the co-impregnation and pyrolysis method. Briefly, $PdCl_2$ (0.047 mmol, 8.40 mg) and $Ni(NO_3)_2{\cdot}6H_2O$ (0.085 mmol, 24.8 mg) were dissolved in 2 mL anhydrous ethanol. Then, the solution of $PdCl_2$ and $Ni(NO_3)_2{\cdot}6H_2O$ was dropwise added to 0.1 g UiO-67-CTAB(3). The suspension was left to age overnight at –4 °C and dried at 100 °C for 2 h in a vacuum oven with a vacuum degree of 0.1 MPa. The dry solid was placed in an alumina boat and pyrolyzed under an air atmosphere in a muffle furnace at 500 °C for 3 h (1 °C/min) to obtain PdNi/UiO-67-CTAB(3)-A500. The PdNi/UiO-67-CTAB(0)-A500, PdNi/UiO-67-CTAB(8)-A500, PdNi/UiO-67-CTAB(13)-A500, and PdNi/UiO-67-CTAB(18)-A500 catalysts

were also synthesized in a similar procedure by the co-impregnation and pyrolysis method. The actual metal (Pd, Ni, and Zr) content of the catalysts as determined by ICP-OES is shown in Table S1.

3.3. Catalytic Activity Evaluation

The hydrogenation of 1,3-butadiene was carried out in a fixed bed using a quartz reactor with an internal diameter of 6 mm at 25–40 °C under atmospheric pressure. Typically, 5 mg of the catalyst was diluted with 500 mg of quartz sand (inert diluent, 40–80 mesh). The catalyst was pretreated in flowing N_2 (8 mL/min) at the reaction temperature for 0.5 h. The reaction gas mixture was 1,3-butadiene/N_2 (1.0 vol.%, 20 mL/min) and H_2 (10 mL/min). The space velocity reached 360,000 mL/(h·g_{cat}) which could eliminate mass-transfer limitation during the 1,3-butadiene hydrogenation. The gas stream at the reactor outlet was analyzed using online GC-6890 (Purkinje General Instrument Co., Ltd., Beijing, China) equipped with an Al_2O_3 capillary column (30 m×0.53 mm×10 mm). Carbon balance was 97% ± 3%. 1,3-butadiene conversion ($X_{1,3\text{-}BD}$) and selectivities (S_i) of butane, 1-butene, *trans*-2-butene, and *cis*-2-butene were calculated using the following equations:

$$X_{1,3-BD}(\%) = \frac{[1,3-BD]_i - [1,3-BD]_f}{[1,3-BD]_i} \times 100$$

$$S_i(\%) = \frac{C_i}{\sum_i C_i} \times 100$$

where [1,3-*BD*]$_i$ is the initial molar flow rate of 1,3-*BD* (mmol/min), [1,3-*BD*]$_f$ is the final molar flow rate of 1,3-*BD* (mmol/min), C_i is the product (such as butane) molar flow rate, and $\sum_i C_i$ is the total product (containing butane, 1-butene, *trans*-2-butene, and *cis*-2-butene) molar flow rate.

4. Conclusions

We have studied the selective hydrogenation of 1,3-butadiene on PdNi/UiO-67-CTAB(n)-A500 (n = 0, 3, 8, 13, 18) catalysts. Catalytic activity strongly depends on the crystal morphology of the UiO-67 template for 1,3-butadiene hydrogenation. The highest catalytic activity was observed over the PdNi/UiO-67-CTAB(3)-A500 catalyst which was synthesized using UiO-67 with a uniform octahedral morphology as the template for 1,3-butadiene selective hydrogenation. Catalytic activity increased with increasing reaction temperature for PdNi/UiO-67-CTAB(3)-A500, whereas the selectivity to total butenes slightly decreased. The higher reaction temperature could promote the secondary hydrogenation of butenes to butane. The 1,3-butadiene conversion and the selectivity of total butenes were 98.4% and 44.8% at 40 °C within 1 h for the PdNi/UiO-67-CTAB(3)-A500 catalyst, respectively. The catalyst of PdNi/UiO-67-CTAB(3)-A500 can be regenerated in flowing N_2 at 200 °C. Carbon deposited on the catalyst during the 1,3-butadiene hydrogenation process was the main reason for its deactivation. This work is valuable for the high-efficiency bimetallic catalyst's development on the selective hydrogenation of 1,3-butadiene.

Supplementary Materials: The following supporting information can be downloaded at https://www.mdpi.com/article/10.3390/molecules29102217/s1, Materials and Methods: materials, characterization and equipment; Table S1: The actual metal content of as-synthesized catalysts analyzed by ICP-OES; Figure S1: TEM photographs and PdNi nanoparticle distributions of PdNi/UiO-67-CTAB(0)-A500 (a,b), PdNi/UiO-67-CTAB(3)-A500 (c,d), PdNi/UiO-67-CTAB(8)-A500 (e,f), PdNi/UiO-67-CTAB(13)-A500 (g,h), and PdNi/UiO-67-CTAB(18)-A500 (i,j).

Author Contributions: Conceptualization, Y.L. and L.L. (Lili Liu); methodology, L.L. (Lili Liu); software, L.L. (Lili Liu); validation, Y.L. and L.L. (Lili Liu); formal analysis, Y.L.; investigation, L.W., M.Z., L.L. (Lei Li) and Y.Z.; resources, Y.L. and L.L. (Lili Liu); data curation, L.W., M.Z., L.L. (Lei Li) and Y.Z.; writing—original draft preparation, L.L. (Lili Liu); writing—review and editing,

Y.L.; visualization, Y.L.; supervision, L.L. (Lili Liu); project administration, Y.L. and L.L. (Lili Liu); funding acquisition, L.L. (Lili Liu). All authors have read and agreed to the published version of the manuscript.

Funding: This research was funded by National Natural Science Foundation of China (grant number 21802104), the Natural Science Foundation of Shandong Province (grant number ZR2017MB056), and the Technology Research and Development Program of Weifang (grant number 2021GX007).

Institutional Review Board Statement: Not applicable.

Informed Consent Statement: Not applicable.

Data Availability Statement: The original contributions presented in the study are included in the article and Supplementary Materials, further inquiries can be directed to the corresponding authors.

Conflicts of Interest: The authors declare no conflicts of interest.

References

1. Yang, Q.; Sun, K.; Xu, Y.; Ding, Z.; Hou, R. Tuning crystal phase of molybdenum carbide catalyst to induce the different selective hydrogenation performance. *Appl. Catal. A Gen.* **2022**, *630*, 118455–118465. [CrossRef]
2. Yang, Q.; Hou, R.; Sun, K. Tuning butene selectivities by Cu modification on Pd-based catalyst for the selective hydrogenation of 1,3-butadiene. *J. Catal.* **2019**, *374*, 12–23. [CrossRef]
3. Hugon, A.; Delannoy, L.; Krafft, J.M.; Louis, C. Selective hydrogenation of 1,3-butadiene in the presence of an excess of alkenes over supported bimetallic gold-palladium catalysts. *J. Phys. Chem. C* **2010**, *114*, 10823–10835. [CrossRef]
4. Hu, N.; Li, X.Y.; Liu, S.M.; Wang, Z.; He, X.K.; Hou, Y.X.; Wang, Y.X.; Deng, Z.; Chen, L.H.; Su, B.L. Enhanced stability of highly-dispersed copper catalyst supported by hierarchically porous carbon for long term selective hydrogenation. *Chin. J. Catal.* **2020**, *41*, 1081–1090. [CrossRef]
5. Hu, C.; Shao, M.; Xiang, M.; Li, S.; Xu, S. The role of hydrogen coverage and location in 1,3-butadiene hydrogenation over Pt/SiO_2. *React. Chem. Eng.* **2020**, *5*, 87–100. [CrossRef]
6. Yan, H.; Cheng, H.; Yi, H.; Lin, Y.; Yao, T.; Wang, C.; Li, J.; Wei, S.; Lu, J. Single-atom Pd_1/graphene catalyst achieved by atomic layer deposition: Remarkable performance in selective hydrogenation of 1,3-butadiene. *J. Am. Chem. Soc.* **2015**, *137*, 10484–10487. [CrossRef] [PubMed]
7. Corstius, O.E.B.; van der Hoeven, J.E.S.; Sunley, G.J.; de Jongh, P.E. Influence of particle size in Pd-catalysed selective hydrogenation of 1,3-butadiene. *J. Catal.* **2023**, *427*, 115103–115111. [CrossRef]
8. Lu, F.; Xu, Y.; Jiang, X.; Liu, Y.; Huang, J.; Sun, D. Biosynthesized Pd/gamma-Al_2O_3 catalysts for low-temperature 1,3-butadiene hydrogenation: The effect of calcination atmosphere. *New J. Chem.* **2017**, *41*, 13036–13042. [CrossRef]
9. Jiang, X.; Lu, F.; Wu, J.; Li, Q.; Sun, D. Bio-inspired n self-doped 3d macroporous carbon supported Pd nanoparticles as an efficient catalyst for selective hydrogenation of 1,3-butadiene. *J. Taiwan Inst. Chem. Eng.* **2022**, *136*, 104391–104396. [CrossRef]
10. Selvakannan, P.R.; Hoang, L.; Kumar, V.V.; Dumbre, D.; Bhargava, S.K. Selective hydrogenation of 1,3-butadiene to 1-butene: Review on catalysts, selectivity, kinetics and reaction mechanism. *Catal. Clean Energy Environ. Sustain.* **2021**, *2*, 205–228.
11. Wang, M.; Wang, Y.; Mou, X.; Lin, R.; Ding, Y. Design strategies and structure-performance relationships of heterogeneous catalysts for selective hydrogenation of 1,3-butadiene. *Chin. J. Catal.* **2022**, *43*, 1017–1041. [CrossRef]
12. Yan, Z.; Cui, L.; Pang, Z.; Shi, K.; Zhang, M.; Guo, J.; Gao, R.; Hao, H. Theoretical study the catalytic performance and mechanism of novel designed single atom catalysts M1/2DMs for 1,3-butadiene hydrogenation. *Appl. Surf. Sci.* **2023**, *617*, 156585–156596. [CrossRef]
13. Huang, J.; Odoom-Wubah, T.; Jing, X.; Sun, D.; Gu, Z.; Li, Q. Plant-mediated synthesis of zinc oxide supported nickel palladium alloy catalyst for the selective hydrogenation of 1,3-butadiene. *ChemCatChem* **2017**, *9*, 870–881. [CrossRef]
14. Yan, Z.; Cui, L.; Shi, K.; Zhang, M.; Pang, Z.; Guo, J.; Gao, R.; Hao, H. Theoretical study the influence of partial substitute noble metal Pd/Ag of PdAg-based catalyst by non-noble metal Ni/Cu for 1,3-Butadiene hydrogenation. *Appl. Surf. Sci.* **2022**, *588*, 152897–152903. [CrossRef]
15. Heemeier, M.; Carlsson, A.F.; Naschitzki, M.; Schmal, M.; Baumer, M.; Freand, H.J. Preparation and characterization of a model bimetallic catalyst: Co–Pd nanoparticles supported on Al_2O_3. *Angew. Chem. Int. Ed.* **2002**, *41*, 4073–4076. [CrossRef]
16. Méndez, F.J.; Piccolo, L.; Solano, R.; Aouine, M.; Villasana, Y.; Guerra, J.; Curbelo, S.; Olivera-Fuentes, C.; Brito, J.L. Promoting effect of ceria on the performance of NiPd/CeO_2-Al_2O_3 catalysts for the selective hydrogenation of 1,3-butadiene in the presence of 1-butene. *New J. Chem.* **2018**, *42*, 11165–11173. [CrossRef]
17. Ma, H.; Xu, X.; Xu, H.; Feng, H.; Xie, Y.; Cheng, D. Understanding composition-dependent catalytic performance of PdAg for the hydrogenation of 1,3-butadiene to 1-butene. *Catal. Commun.* **2021**, *149*, 106255–106260. [CrossRef]
18. Lu, F.; Sun, D.; Jiang, X. Plant-mediated synthesis of AgPd/γ-Al_2O_3 catalysts for selective hydrogenation of 1,3-butadiene at low temperature. *New J. Chem.* **2019**, *43*, 13891–13898. [CrossRef]
19. Lv, C.Q.; Liu, J.H.; Guo, Y.; Wang, G.C. Selective hydrogenation of 1,3-butadiene over single Pt_1/Cu(1 1 1) model catalysts: A DFT study. *Appl. Surf. Sci.* **2019**, *466*, 946–955. [CrossRef]

20. Liu, L.; Yu, L.; Zhou, X.; Xin, C.; Sun, S.; Liu, Z.; Zhang, J.; Liu, Y.; Tai, X. Comparative study of Pd–Ni bimetallic catalysts supported on UiO-66 and UiO-66-NH_2 in selective 1,3-butadiene hydrogenation. *Nanomaterials* **2022**, *12*, 1484. [CrossRef]
21. Hou, R.; Porosoff, M.D.; Chen, J.G.; Wang, T. Effect of oxide supports on Pd-Ni bimetallic catalysts for 1,3-butadiene hydrogenation. *Appl. Catal. A-Gen.* **2015**, *490*, 17–23. [CrossRef]
22. Sarkany, A.; Zsoldos, Z.; Stefler, G.; Hightower, J.W.; Guczi, L. Promoter effect of Pd in hydrogenation of 1,3-butadiene over Co-Pd catalysts. *J. Catal.* **1995**, *157*, 179–189. [CrossRef]
23. Liu, L.; Zhou, X.; Guo, L.; Yan, S.; Li, Y.; Jiang, S.; Tai, X. Bimetallic Au–Pd alloy nanoparticles supported on MIL-101(Cr) as highly efficient catalysts for selective hydrogenation of 1,3-butadiene. *RSC Adv.* **2020**, *10*, 33417–33427. [CrossRef] [PubMed]
24. Huang, H.; Dai, J.; Liu, X.; Tan, K.B.; Huang, J.; Zhan, G.; Li, Q.; Acquisition, F. Waste eggshell with naturally-functionalized sulfonic groups as excellent support for loading Pd and Ag nanoparticles towards enhanced 1,3-butadiene hydrogenation. *Mol. Catal.* **2021**, *510*, 111689–111698. [CrossRef]
25. Feng, X.; Wu, D.; Shen, X.; Guo, Y.; Lv, Y.; Xu, A.; Li, X. Activation of sulfite by metal-organic framework-derived cobalt nanoparticles for organic pollutants removal. *J. Environ. Sci.* **2023**, *124*, 350–359. [CrossRef]
26. Han, Y.C.; Liu, M.L.; Sun, L.; Li, X.C.; Yao, Y.; Zhang, C.; Ding, S.Y.; Liao, H.G.; Zhang, L.; Fan, F.R.; et al. A general strategy for overcoming the trade-off between ultrasmall size and high loading of MOF-derived metal nanoparticles by millisecond pyrolysis. *Nano Energy* **2022**, *97*, 107125–107134. [CrossRef]
27. Torkashvand, Z.; Sepehrmansourie, H.; Zolfigol, M.A.; As'Habi, M.A. Application of Ti-MOF-UR as a new porous catalyst for the preparation of pyrazolo [3,4-*b*]quinoline and pyrazolo [4,3-*e*]pyridines. *Mol. Catal.* **2023**, *541*, 113107–113118. [CrossRef]
28. Chen, Y.; Liu, A.; Liu, P.; Zhang, Z.; Yu, F.; Qi, W.; Li, B. Application of copper(II)-organic frameworks bearing dilophine derivatives in photocatalysis and guest separation. *Inorg. Chem.* **2022**, *61*, 16009–16019. [CrossRef] [PubMed]
29. Qin, L.; Ru, R.; Mao, J.; Meng, Q.; Fan, Z.; Li, X.; Zhang, G. Assembly of MOFs/polymer hydrogel derived Fe_3O_4-CuO@hollow carbon spheres for photochemical oxidation: Freezing replacement for structural adjustment. *Appl. Catal. B-Environ.* **2020**, *269*, 118754–118763. [CrossRef]
30. Wei, Q.; Sun, Y.; Wang, S.; Hu, Z.; Liu, Q.; Zheng, X. Construction of highly dispersed Pt single sites and high-efficiency heterocatalysis silylation of alcohols with silanes. *Nano Res.* **2023**, *16*, 4643–4649. [CrossRef]
31. Zhang, C.; Gao, H.; Hai, G.; Zeng, Y.; Wang, X.; Xing, L.; Zhao, J.; Wang, G.; Shu, X. Base-free catalytic aerobic oxidation of mercaptans over MOF-derived Co/CN catalyst with controllable composition and structure. *J. Colloid Interface Sci.* **2022**, *607*, 1836–1848. [CrossRef]
32. Wang, T.; Zhou, Q.Y.; Wang, X.J.; Zheng, J.; Li, X.G. MOF-derived surface modified Ni nanoparticles as an efficient catalyst for the hydrogen evolution reaction. *J. Mater. Chem. A* **2015**, *3*, 16435–16439. [CrossRef]
33. Chong, L.; Wen, J.; Kubal, J.; Sen, F.G.; Zou, J.; Greeley, J.; Chan, M.; Barkholtz, H.; Ding, W.; Liu, D.-J. Ultralow-loading platinum-cobalt fuel cell catalysts derived from imidazolate frameworks. *Science* **2018**, *362*, 1276–1281. [CrossRef]
34. Zeng, D.; Li, Y.; Ma, H.; Cui, F.; Zhang, J. CuO@NiO nanoparticles derived from metal-organic framework precursors for the deoxygenation of fatty acids. *ACS Sustain. Chem. Eng.* **2021**, *9*, 15612–15622. [CrossRef]
35. Zhao, X.; Zhou, Y.; Liang, Q.; Zhou, M.; Li, Z.; Xu, S. Coupling MOF-derived titanium oxide with $CdIn_2S_4$ formed 2D/3D core–shell heterojunctions with enhanced photocatalytic performance. *Sep. Purif. Technol.* **2021**, *279*, 119765–119779. [CrossRef]
36. Zhang, H.; Jia, M.; Tong, J.; Peng, H.; Xiang, Y.; Chen, Z.; Xu, Z.; Yang, Z.; Xiong, W. Coupling effects between metal–organic framework derivatives and oxygen-deficient TiO_2 nanotubes: Identified charge-transfer processes and photoelectric synergistic effect. *Environ. Sci. Nano* **2023**, *10*, 1993–2009. [CrossRef]
37. Wang, H.; Sun, C.; Zhu, E.; Shi, C.; Yu, J.; Xu, M. Core-shell MOF-derived Fe_3C-Co-NC as high-performance ORR/OER bifunctional catalyst. *J. Alloys Compd.* **2023**, *948*, 169728–169737. [CrossRef]
38. Boroujerdian, M.; Rahimi, S.; Nezhad, S.M.; Pourmousavi, S.A.; Zare, E.N.; Salimi, F.; Amirahmadi, F.; Daneshgar, H. $CoFe_2O_4$@SiO_2–NH_2@MOF-5 magnetic nanocatalyst for the synthesis of biologically active quinazoline derivatives. *Environ. Res.* **2023**, *236*, 116708–116722. [CrossRef] [PubMed]
39. Lei, J.; Wang, S.; Li, J.; Xu, Y.; Li, S. Different effect of Y (Y = Cu, Mn, Fe, Ni) doping on Co_3O_4 derived from Co-MOF for toluene catalytic destruction. *Chem. Eng. Sci.* **2022**, *251*, 117436–117444. [CrossRef]
40. Lei, J.; Wang, P.; Wang, S.; Li, J.; Xu, Y.; Li, S. Enhancement effect of Mn doping on Co_3O_4 derived from Co-MOF for toluene catalytic oxidation. *Chin. J. Chem. Eng.* **2022**, *52*, 1–9. [CrossRef]
41. Wang, Z.; Bo, K.; Wang, Y.; Wang, Y. Eutectic salts assisted synthesis of MOF-derived porous carbon as Pt-Sn catalyst support for ethanol oxidation reaction. *Int. J. Hydrogen Energy* **2022**, *47*, 18285–18293. [CrossRef]
42. Wang, Y.; Bi, F.; Wang, Y.; Jia, M.; Tao, X.; Jin, Y.; Zhang, X. MOF-derived CeO_2 supported Ag catalysts for toluene oxidation: The effect of synthesis method. *Mol. Catal.* **2021**, *515*, 111922–111932. [CrossRef]
43. Beiranvand, M.; Habibi, D.; Khodakarami, H. Novel UiO-NH_2-like Zr-based MOF (Basu-DPU) as an excellent catalyst for preparation of new 6*H*-chromeno [4,3-*b*]quinolin-6-ones. *ACS Omega* **2023**, *8*, 25924–25937. [CrossRef]
44. Zhu, Y.; Lv, Z. Determination of water-soluble nitrate ions in PM2.5 particles using UiO-67 modified glassy carbon electrode. *Int. J. Electrochem. Sci.* **2022**, *17*, 2–12. [CrossRef]
45. Liu, L.; Tai, X.; Zhou, X.; Liu, L.; Zhang, X.; Ding, L.; Zhang, Y. Au-Pt bimetallic nanoparticle catalysts supported on UiO-67 for selective 1,3-butadiene hydrogenation. *J. Taiwan Inst. Chem. Eng.* **2020**, *114*, 220–227. [CrossRef]

46. Samperisi, L.; Jaworski, A.; Kaur, G.; Lillerud, K.P.; Zou, X.; Huang, Z. Probing molecular motions in metal-organic frameworks by three dimensional electron diffraction. *J. Am. Chem. Soc.* **2021**, *143*, 17947–17952. [CrossRef] [PubMed]
47. Xu, F.; Dong, M.; Gou, W.; Li, J.; Qin, Z.; Wang, J.; Fan, W. Rapid tuning of ZSM-5 crystal size by using polyethylene glycol or colloidal silicalite-1 seed. *Microporous Mesoporous Mater.* **2012**, *163*, 192–200. [CrossRef]
48. Li, J.; He, L.; Liu, Q.; Ren, Y.; Jiang, H. Visible light-driven efficient palladium catalyst turnover in oxidative transformations within confined frameworks. *Nat. Commun.* **2022**, *13*, 928–940. [CrossRef] [PubMed]
49. Lin, S.; Cairnie, D.R.; Chakraborty, A.; Cai, M.; Morris, A.J. Photoelectrochemical alcohol oxidation by mixed-linker metal organic frameworks. *Faraday Discuss.* **2021**, *225*, 371–383. [CrossRef]
50. Zhang, L.Y.; Yang, J.J.; Yan, Y.L. Novel adsorption-photocatalysis integrated bismuth tungstate modified layered mesoporous titanium dioxide (Bi_2WO_6/LM-TiO_2) composites. *Opt. Mater.* **2022**, *130*, 112581–112590. [CrossRef]
51. Lu, J.; Wang, Y.; Sun, C.; Zhao, T.; Zhao, J.; Wang, Z.; Liu, W.; Wu, S.; Shi, M.; Bu, L. Novel synthesis and catalytic performance of hierarchical MOR. *New J. Chem.* **2021**, *45*, 8629–8638. [CrossRef]
52. Wang, L.; Lin, X.; Sheng, Y.; Zhu, H.; Li, Z.; Su, Z.; Yu, R.; Zhang, S. Synthesis of a crystalline zeolitic imidazole framework-8 nano-coating on single environment-sensitive viral particles for enhanced immune responsed. *Nanoscale Adv.* **2023**, *5*, 1433–1449. [CrossRef]
53. Sadeh, P.; Zeinali, S.; Rastegari, B.; Najafipour, I. Size optimization of mesoporous β-cyclodextrin metal-organic frameworks as bio-MOFs. *J. Cryst. Growth* **2023**, *620*, 127348–127354. [CrossRef]
54. Ahmadi, H.; Khalaj, G.; Soleymani, F.; Moalem, M.; Pourabdollah, M.; Mahmoudan, M. Electrochemical synthesis and characterization of Cu_2O nanoparticles: Effect of electrolyte composition. *J. Solid State Electrochem.* **2023**, 1–13. [CrossRef]
55. He, P.; Li, Y.; Cai, K.; Xiong, X.; Lv, J.; Wang, Y.; Huang, S.; Ma, X. Nano-assembled mordenite zeolite with tunable morphology for carbonylation of dimethyl ether. *ACS Appl. Nano Mater.* **2020**, *3*, 6460–6468. [CrossRef]
56. Jubeer, E.M.; Manthrammel, M.A.; Shkir, M.; Subha, P.A.; Yahia, I.S.; Alfaify, S.A. Microwave assisted synthesis of quantum dots like ZnS nanoparticles for optoelectronic applications: An effect of CTAB concentrations. *Optik* **2021**, *240*, 166812–166820. [CrossRef]
57. Ping, C.; Chen, X.; Qin, F.; Ma, W. Effect of preparation conditions on the morphology and catalytic performance of nickel phosphate nanotubes. *Cryst. Res. Technol.* **2022**, *57*, 2100273–2100281. [CrossRef]
58. Liu, L.; Zhou, X.; Xin, C.; Zhang, B.; Zhang, G.; Li, S.; Liu, L.; Tai, X. Efficient oxidation of benzyl alcohol into benzaldehyde catalyzed by graphene oxide and reduced graphene oxide supported bimetallic Au–Sn catalysts. *RSC Adv.* **2023**, *13*, 23648–23658. [CrossRef] [PubMed]
59. Liu, L.; Han, Z.; Lv, Y.; Xin, C.; Zhou, X.; Yu, L.; Tai, X. MIL-100(Fe) supported PtCo nanoparticles as active and selective heterogeneous catalysts for hydrogenation of 1,3-butadiene. *ChemistryOpen* **2022**, *11*, e202100288. [CrossRef]
60. Ren, H.; Cheng, L.; Yang, J.; Zhao, K.; Zhai, Q.; Li, Y. Recyclable and reusable chiral α, α-L-diaryl prolinol heterogeneous catalyst grafting to UiO-67 for enantioselective hydration/aldol/oxa-Diels Alder domino reaction. *Catal. Commun.* **2021**, *149*, 106249–106254. [CrossRef]
61. Melillo, A.; García-Aboal, R.; Navalón, S.; Atienzar, P.; Ferrer, B.; Álvaro, M.; García, H. Photoactive Zr and Ti metal-organic-frameworks for solid-state solar cells. *ChemPhysChem* **2021**, *22*, 842–848. [CrossRef] [PubMed]
62. Han, X.; Li, M.; Chang, X.; Hao, Z.; Chen, J.; Pan, Y.; Kawi, S.; Ma, X. Hollow structured Cu@ZrO_2 derived from Zr-MOF for selective hydrogenation of CO_2 to methanol. *J. Energy Chem.* **2022**, *71*, 277–287. [CrossRef]
63. Palani, R.; Wu, Y.S.; Wu, S.H.; Jose, R.; Yang, C.C. Metal-organic framework-derived ZrO_2/$NiCo_2O_4$/graphene mesoporous cake-like structure as enhanced bifunctional electrocatalytic cathodes for long life Li-O_2 batteries. *Electrochim. Acta* **2022**, *412*, 140147–140159. [CrossRef]
64. Alqarni, D.S.; Marshall, M.; Gengenbach, T.R.; Lippi, R.; Chaffee, A.L. Rh/ZrO_2@C(MIL) catalytic activity and TEM images. CO_2 conversion performance and structural systematic evaluation of novel catalysts derived from Zr-MOF metallated with Ru, Rh, Pd or In. *Microporous Mesoporous Mater.* **2022**, *336*, 111855–111960. [CrossRef]
65. Numpilai, T.; Kidkhunthod, P.; Cheng, C.K.; Wattanakit, C.; Chareonpanich, M.; Limtrakul, J.; Witoon, T. CO_2 hydrogenation to methanol at high reaction temperatures over In_2O_3/ZrO_2 catalysts: Influence of calcination temperatures of ZrO_2 support. *Catal. Today* **2021**, *375*, 298–306. [CrossRef]
66. Martínez-Martínez, R.; Juárez-López, G.; García-Hipólito, M.; Díaz, J.B.; Téllez, S.C.; Aguilar-Frutis, M.A.; Flores, G.A.; Falcony, C. Blue and bluish-white colors from the luminescent ZrO_2 and ZrO_2: Al^{3+} films prepared by the USP method. *Mater. Res. Express* **2021**, *8*, 016201–016214. [CrossRef]
67. Liu, L.; Zhou, X.; Liu, L.; Jiang, S.; Li, Y.; Guo, L.; Yan, S.; Tai, X. Heterogeneous bimetallic Cu-Ni nanoparticle-supported catalysts in the selective oxidation of benzyl alcohol to benzaldehyde. *Catalysts* **2019**, *9*, 538. [CrossRef]
68. Gao, Y.; Meng, X.; Huang, S.; Wu, H.; Jiang, L.; Zhou, Y.; Song, Y.; Diao, Y. Effects of MgO doping in Pd/γ-Al_2O_3 catalysts for the hydrogenation of perfluoro olefin. *Mol. Catal.* **2024**, *552*, 113652–113661. [CrossRef]
69. Zhou, D.; Chen, X.; Liang, B.; Fan, X.; Wei, X.; Liang, J.; Wang, L. Embedding MIL-100(Fe) with magnetically recyclable Fe_3O_4 nanoparticles for highly efficient esterification of diterpene resin acids and the associated kinetics. *Microporous Mesoporous Mater.* **2019**, *289*, 109615–109624. [CrossRef]

70. Liu, L.; Tai, X.; Zhou, X.; Hou, J.; Zhang, Z. Bimetallic Au-Ni alloy nanoparticles in a metal-organic framework (MIL-101) as effificient heterogeneous catalysts for selective oxidation of benzyl alcohol into benzaldehyde. *J. Alloys Compd.* **2019**, *790*, 326–336. [CrossRef]
71. Zhang, X.; Li, W.; Zhou, Z.; Chen, K.; Wu, M.; Yuan, L. High dispersed Pd supported on CeO_2 (1 0 0) for CO oxidation at low temperature. *Mol. Catal.* **2021**, *508*, 111580–111587. [CrossRef]
72. Osuga, R.; Takeuchi, T.; Sawada, M.; Kunitake, Y.; Matsumoto, T.; Yasuda, S.; Onozuka, H.; Tsutsuminai, S.; Kondo, J.N.; Gies, H.; et al. Fabrication of AEI-type aluminosilicate catalyst with sheet-like morphology for direct conversion of propene to butenes. *Catal. Sci. Technol.* **2021**, *11*, 5839–5848. [CrossRef]
73. Li, M.; Zhou, H.; Zhang, L.; Han, J.; Wang, G.; Fan, F.; Wang, T.; Zhang, X.; Fu, Y. Size and morphology control of two-dimensional metal-organic frameworks through coordination modulation. *Microporous Mesoporous Mater.* **2023**, *348*, 112379–112385. [CrossRef]
74. Wu, M.; Miao, M.; Li, W.; Zhang, X.; Zhang, L.; Zhen, T.; Fu, Y.; Jin, J.; Yuan, L. Metal-organic framework-derived one-dimensional Pd@CeO_2 catalysts with enhanced activity for methane oxidation. *Fuel* **2023**, *331*, 125575–125584. [CrossRef]
75. Zou, H.H.; Yuan, C.Z.; Zou, H.Y.; Cheang, T.Y.; Zhao, S.J.; Qazi, U.Y.; Zhong, S.L.; Wang, L.; Xu, A.W. Bimetallic phosphide hollow nanocubes derived from a prussian-blue-analog used as highperformance catalysts for the oxygen evolution reaction. *Catal. Sci. Technol.* **2017**, *7*, 1549–1555. [CrossRef]
76. Lu, W.; Wang, J.; Ma, Z.; Chen, C.; Liu, Y.; Hou, B.; Li, D.; Wang, B. Classifying and understanding the role of carbon deposits on cobalt catalyst for Fischer-Tropsch synthesis. *Fuel* **2023**, *332*, 126115–126121. [CrossRef]
77. Duan, J.; He, Z.; Ma, Z.; Yue, J.; Wang, W.; Li, C. The composite of Zr-doped TiO2 and MOF-derived metal oxide for oxidative removal of formaldehyde at the room temperature. *Microporous Mesoporous Mater.* **2022**, *336*, 111892–111901. [CrossRef]
78. Mo, W.L.; Ren, Y.; Ma, Y.; Guo, J.; Feng, Z.H.; Zhang, S.P.; Yang, X.Q. Structure characteristics and removal behavior of the deposited carbon on Ni-Al2O3 catalyst for CO_2 reforming of CH_4. *Processes* **2023**, *11*, 2968. [CrossRef]
79. Chai, J.; Pestman, R.; Chiang, F.K.; Men, Z.; Wang, P.; Hensen, E.J.M. Influence of carbon deposits on Fe-carbide for the Fischer-Tropsch reaction. *J. Catal.* **2022**, *416*, 289–300. [CrossRef]
80. Xu, Y.; Ma, D.; Yu, J.; Jiang, X.; Huang, J.; Sun, D. Plant-mediated synthesis of Pd catalysts toward selective hydrogenation of 1,3-butadiene: The effect of halide ions. *Ind. Eng. Chem. Res.* **2017**, *56*, 10623–10630. [CrossRef]
81. Pattamakomsan, K.; Ehret, E.; Morfin, F.; Gelin, P.; Jugnet, Y.; Prakash, S.; Bertolini, J.C.; Panpranot, J.; Aires, F.J.C.S. Selective hydrogenation of 1,3-butadiene over Pd and Pd-Sn catalysts supported on different phases of alumina. *Catal. Today* **2011**, *164*, 28–33. [CrossRef]
82. Asedegbega-Nieto, E.; Iglesias-Juez, A.; Di Michiel, M.; Fernandez-Garcia, M.; Rodriguez-Ramos, I.; Guerrero-Ruiz, A. Dynamics of Pd subsurface hydride formation and their impact on the selectivity control for selective butadiene hydrogenation reaction. *Nanomaterials* **2023**, *13*, 1099. [CrossRef]
83. van der Hoeven, J.E.S.; Jelic, J.; Olthof, L.A.; Totarella, G.; van Dijk-Moes, R.J.A.; Krafft, J.M.; Louis, C.; Studt, F.; van Blaaderen, A.; de Jongh, P.E. Unlocking synergy in bimetallic catalysts by core–shell design. *Nat. Mater.* **2021**, *20*, 1216–1220. [CrossRef]
84. Odoom-Wubah, T.; Li, Q.; Chen, M.; Fang, H.; Asare Bediako, B.B.; Adilov, I.; Huang, J.; Li, Q. Influence of preparation methods on the catalytic activity of Pd–Cu/Mn_2O_3 catalyst in the hydrogenation of 1,3-butadiene. *ACS Omega* **2019**, *4*, 1300–1310. [CrossRef]
85. Yi, H.; Du, H.; Hu, Y.; Yan, H.; Jiang, H.L.; Lu, J. Precisely controlled porous alumina overcoating on Pd catalyst by atomic layer deposition: Enhanced selectivity and durability in hydrogenation of 1,3-butadiene. *ACS Catal.* **2015**, *5*, 2735–2739. [CrossRef]
86. Sárkány, A. Features of deposit formation from 1,3-butadiene over Pd catalysts. *React. Kinet. Catal. Lett.* **1999**, *68*, 153–163. [CrossRef]
87. Frusteri, F.; Spadaro, L.; Arena, F.; Chuvilin, A. TEM evidence for factors affecting the genesis of carbon species on bare and K-promoted Ni/MgO catalysts during the dry reforming of methane. *Carbon* **2002**, *40*, 1063–1070. [CrossRef]
88. Liu, F.; Li, H.; Fu, Q.; He, X.; Zhang, W. ZrSi2-SiC/SiC gradient coating of micro-structure and anti-oxidation property on C/C composites prepared by SAPS. *Coatings* **2022**, *12*, 1377. [CrossRef]